High-Temperature Charge-Stripe Correlations in $La_{1.675}Eu_{0.2}Sr_{0.125}CuO_4$

Qisi Wang,[1,*] M. Horio,[1] K. von Arx,[1] Y. Shen,[2] D. John Mukkattukavil,[3] Y. Sassa,[4] O. Ivashko,[1] C. E. Matt,[5,1] S. Pyon,[6] T. Takayama,[6] H. Takagi,[6] T. Kurosawa,[7] N. Momono,[7,8] M. Oda,[7] T. Adachi,[9] S. M. Haidar,[10] Y. Koike,[10] Y. Tseng,[5] W. Zhang,[5] J. Zhao,[2,11] K. Kummer,[12] M. Garcia-Fernandez,[13] Ke-Jin Zhou,[13] N. B. Christensen,[14] H. M. Rønnow,[15] T. Schmitt,[5] and J. Chang[1,†]

[1]*Physik-Institut, Universität Zürich, Winterthurerstrasse 190, CH-8057 Zürich, Switzerland*
[2]*State Key Laboratory of Surface Physics and Department of Physics, Fudan University, Shanghai 200433, China*
[3]*Department of Physics and Astronomy, Uppsala University, Box 516, SE-751 20 Uppsala, Sweden*
[4]*Department of Physics, Chalmers University of Technology, SE-412 96 Göteborg, Sweden*
[5]*Swiss Light Source, Photon Science Division, Paul Scherrer Institut, CH-5232 Villigen PSI, Switzerland*
[6]*Department of Advanced Materials, University of Tokyo, Kashiwa 277-8561, Japan*
[7]*Department of Physics, Hokkaido University, Sapporo 060-0810, Japan*
[8]*Department of Applied Sciences, Muroran Institute of Technology, Muroran 050-8585, Japan*
[9]*Department of Engineering and Applied Sciences, Sophia University, Tokyo 102-8554, Japan*
[10]*Department of Applied Physics, Tohoku University, Sendai 980-8579, Japan*
[11]*Collaborative Innovation Center of Advanced Microstructures, Nanjing 210093, China*
[12]*European Synchrotron Radiation Facility, 71 Avenue des Martyrs, 38043 Grenoble, France*
[13]*Diamond Light Source, Harwell Campus, Didcot, Oxfordshire OX11 0DE, United Kingdom*
[14]*Department of Physics, Technical University of Denmark, DK-2800 Kongens Lyngby, Denmark*
[15]*Institute of Physics, École Polytechnique Fedérale de Lausanne (EPFL), CH-1015 Lausanne, Switzerland*

(Received 26 November 2019; revised manuscript received 2 March 2020; accepted 14 April 2020; published 7 May 2020)

We use resonant inelastic x-ray scattering to investigate charge-stripe correlations in $La_{1.675}Eu_{0.2}Sr_{0.125}CuO_4$. By differentiating elastic from inelastic scattering, it is demonstrated that charge-stripe correlations precede both the structural low-temperature tetragonal phase and the transport-defined pseudogap onset. The scattering peak amplitude from charge stripes decays approximately as T^{-2} towards our detection limit. The in-plane integrated intensity, however, remains roughly temperature independent. Therefore, although the incommensurability shows a remarkably large increase at high temperature, our results are interpreted via a single scattering constituent. In fact, direct comparison to other stripe-ordered compounds ($La_{1.875}Ba_{0.125}CuO_4$, $La_{1.475}Nd_{0.4}Sr_{0.125}CuO_4$, and $La_{1.875}Sr_{0.125}CuO_4$) suggests a roughly constant integrated scattering intensity across all these compounds. Our results therefore provide a unifying picture for the charge-stripe ordering in La-based cuprates. As charge correlations in $La_{1.675}Eu_{0.2}Sr_{0.125}CuO_4$ extend beyond the low-temperature tetragonal and pseudogap phase, their emergence heralds a spontaneous symmetry breaking in this compound.

DOI: 10.1103/PhysRevLett.124.187002

Unconventional superconductivity is often associated with competing intertwined order parameters. For underdoped cuprate superconductors, the omnipresence of charge ordering (CO) has been established [1–5]. The observation of different ordering vectors, however, opens the possibility of multiple ordering susceptibilities. It is therefore pivotal to investigate the different types of charge ordering tendencies. In this context, the La-based cuprates constitute an important group of compounds. In fact, spin-charge stripe order was first discovered in $La_{1.475}Nd_{0.4}Sr_{0.125}CuO_4$ (LNSCO) [1] and subsequently studied intensively in the $La_{2-x}Ba_xCuO_4$ system [6–8]. These two compounds share a low-temperature tetragonal (LTT) crystal structure that appears concomitantly with charge ordering. The LTT phase is characterized by tilting of the CuO_6 octahedra with the rotation axis along the copper-oxygen bond directions [see Figs. 1(a) and 1(b)]. It breaks C_4 symmetry within individual CuO_2 planes, consistently with charge-stripe ordering. The potential link between charge-stripe ordering and the LTT phase has therefore been the subject of many experiments [1,2,8–10]. A fundamental question is whether the LTT structure is a consequence or trigger of stripe order. The original scattering experiments found that the LTT and stripe order parameters have identical onsets in temperature [1,6]. As the LTT order parameter grows faster, stripe order has been viewed as a secondary effect. Starting from $La_{1.875}Ba_{0.125}CuO_4$ (LBCO), another set of experiments has traced stripe ordering as the LTT phase is suppressed by hydrostatic pressure [9], temperature [11], or Sr for Ba substitution [12–14]. In all cases, it is found that charge-stripe order emerges spontaneously outside

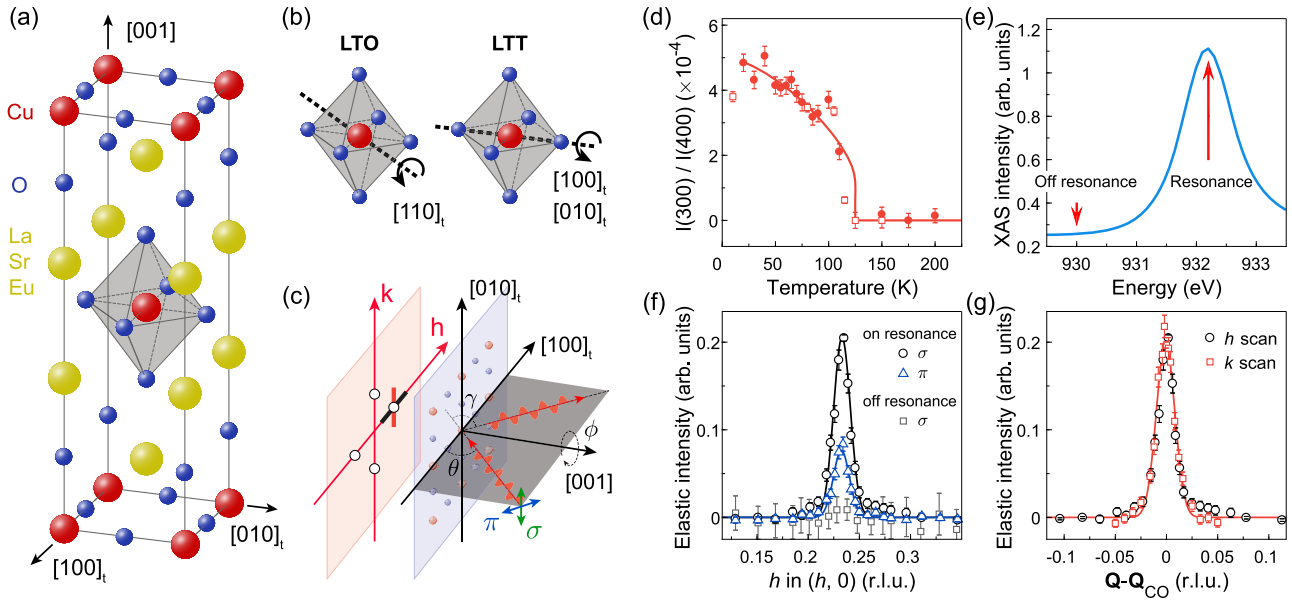

FIG. 1. Crystal structure and low-temperature charge order in LESCO. (a) Crystal structure of LESCO in the high-temperature tetragonal phase. Upon cooling, it first undergoes a structural transition to the low-temperature orthorhombic (LTO) phase then enters the LTT phase at lower temperature. (b) Distortions of the CuO_6 octahedra in the LTO and LTT phases. (c) Schematic of the scattering geometry of the RIXS experiments. The incident angle θ is defined with respect to the CuO_2 plane. The black open circles denote the in-plane position of the CO reflections. (d) Temperature dependence of (3,0,0) structural peak intensity, measured with nonresonant 8.048 keV x rays, characterizes the development of LTT phase. The intensity is normalized to the amplitude of (4,0,0) Bragg peak. The filled and open symbols represent data measured by counting at both the peak and background positions or by fitting longitudinal scans, respectively. (e) Normal incidence x-ray absorption spectroscopy (XAS) spectrum obtained with σ polarized light. (f) Momentum scans (**Q** scans) of the elastic intensity through the CO peak position along h measured with σ and π polarizations and at the off-resonance energy (930.0 eV) indicated in (e). (g) Elastic **Q** scans along h and k directions as indicated by the black and red thick lines in (c), respectively. Solid lines in (f) and (g) are Gaussian fits. Error bars are defined by counting statistics or estimated from systematic uncertainties throughout the Letter [17].

the LTT crystal lattice phase. A prominent exception is $La_{1.675}Eu_{0.2}Sr_{0.125}CuO_4$ (LESCO) that has the highest LTT onset temperature [$T_s \sim 125$ K; see Fig. 1(d)] and where stripe order, probed by resonant elastic x-ray scattering (REXS), appears only below 80 K [10,15,16]. This pronounced temperature "gap" between the LTT and REXS-defined stripe order onsets suggests no fundamental correlation between the two. The lack of universal behavior across the La-based cuprates has impeded broader conclusions on the stripe ordering.

Here, we present a high-resolution resonant inelastic x-ray scattering (RIXS) study of $La_{1.675}Eu_{0.2}Sr_{0.125}CuO_4$ (LESCO-1/8). By filtering inelastic from elastic processes, it is shown that charge correlations survive beyond both the LTT phase and the pseudogap onset T^* defined by transport experiments [27]. This demonstrates that, in this compound, stripe correlations appear spontaneously in the absence of LTT and pseudogap phase. The charge-stripe diffraction peak amplitude decays approximately as T^{-2} as our RIXS detection limit is approached in the high-temperature limit. The diffraction intensity integrated within the probed momentum space, by contrast, appears roughly temperature independent. Although the charge ordering wave vector exhibits a large shift at high temperature, the constant integrated intensity suggests a single ordering mechanism. Finally, we provide evidence for an approximately constant in-plane integrated intensity across all known 1/8-doped stripe-ordered cuprate systems.

Single crystals of LESCO, LNSCO, LBCO, and $La_{1.875}Sr_{0.125}CuO_4$ (LSCO) were grown using a floating zone method. RIXS experiments were carried out at the ADRESS [28,29], I21, and ID32 beam lines at the Swiss Light Source (SLS) at the Paul Scherrer Institut, Diamond Light Source, and European Synchrotron Radiation Facility (ESRF), respectively. Energy resolution, expressed in standard Gaussian deviation ranges from $\sigma_G \approx 19$ to 48 meV for experiments on LESCO. A complete discussion of experimental configurations and resolution linewidth profiles is given in the Supplemental Material [17]. Given the quasi-two-dimensional character of this system, only the in-plane momentum is considered and varied through the incident light θ and sample azimuthal ϕ angles [Fig. 1(c)]. Both linear vertical (σ) and linear horizontal (π) incident light polarizations [Fig. 1(c)] were used. All crystals were cleaved *in situ* by a standard top-post technique. Wave vector **Q** at (q_x, q_y, q_z) is defined as $(h, k, \ell) = (q_x a/2\pi, q_y b/2\pi, q_z c/2\pi)$ reciprocal lattice

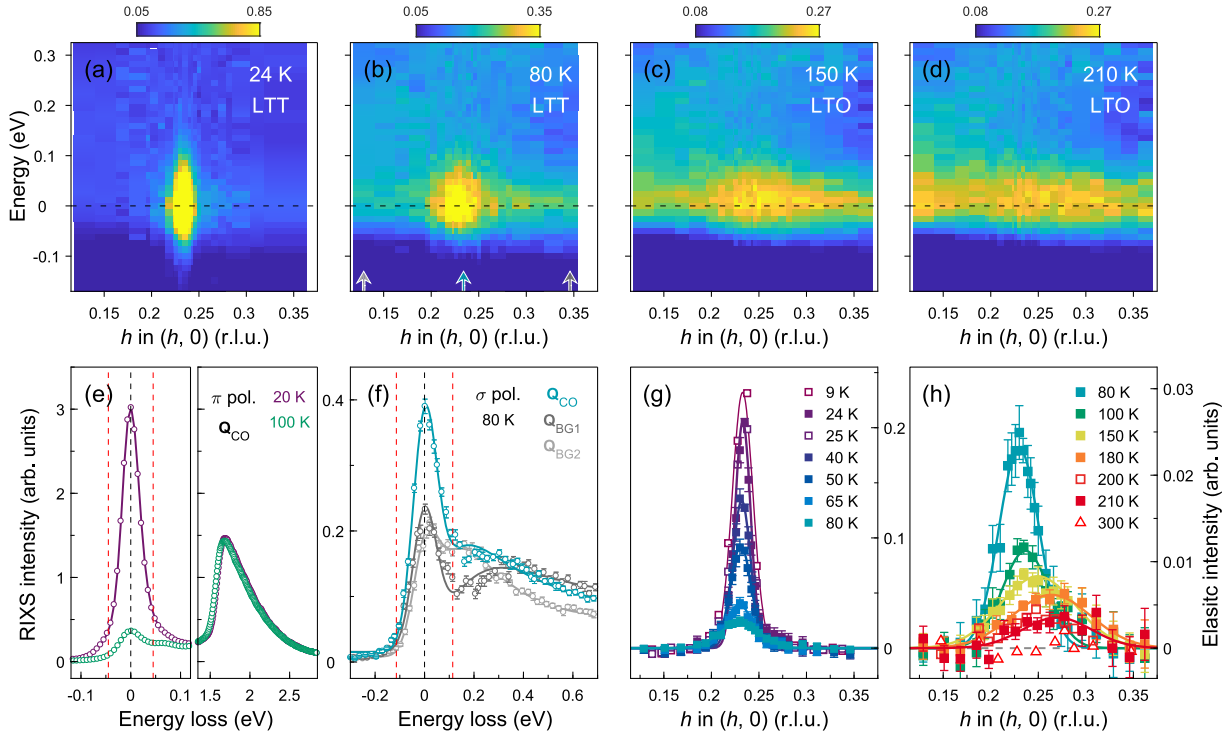

FIG. 2. Temperature evolution of the charge-stripe order. (a)–(d) Intensity distribution maps of the raw RIXS spectra in the energy-momentum space through the CO peak for different temperatures. (e) High-resolution RIXS spectra obtained near $\mathbf{Q}_{\mathrm{CO}}$ with π polarization for indicated temperatures. Data near the elastic line (left-hand part) and *dd* excitations (right-hand part) are shown on different energy scales for clarity. (f) Representative RIXS spectra collected at 80 K. The blue, black, and light gray open circles represent data measured at the CO peak and background positions indicated by the arrows in (b) [$\mathbf{Q}_{\mathrm{BG1}} = (0.346, 0)$, $\mathbf{Q}_{\mathrm{BG2}} = (0.129, 0)$], respectively. The red dashed lines in (e) and (f) mark the energy window of the elastic intensity integration. (g),(h) Elastic scans along h at various temperatures with linear backgrounds subtracted. The filled and open symbols represent data obtained at ADRESS and I21, respectively. Solid lines in (g) and (h) are Gaussian fits to the data.

units (r.l.u.) using pseudotetragonal notation, with $a \approx b \approx 3.79$ Å and $c \approx 13.1$ Å for LESCO.

Charge-stripe order in the La-based cuprates manifests itself by satellite peaks at the wave vectors $\mathbf{Q} = \boldsymbol{\tau} + \mathbf{Q}_{\mathrm{CO}}$, where $\boldsymbol{\tau}$ represents fundamental Bragg reflections and $\mathbf{Q}_{\mathrm{CO}} = (\delta_a, 0, \delta_c)$ and $(0, \delta_b, \delta_c)$. The in-plane incommensurability $\delta = \delta_a = \delta_b$ is close to $1/4$, and weak out-of-plane antiphase correlations imply broad diffraction maxima at $\delta_c = 1/2$ [8,14]. Cu L-edge [~932.2 eV, Fig. 1(e)] RIXS permits resonant x-ray diffraction (XRD) with a well-defined energy resolution. Such resonant energy-resolved XRD data recorded on LESCO-1/8 at $T = 24$ K are shown in Figs. 1(f) and 1(g). It reveals—consistent with previous reports [10,15,16]—that (i) the low-temperature charge order incommensurability is $\delta = 0.233$ [15,30], (ii) the electronic ordering is probed on the resonance only [11], (iii) the reflection is most intense using incident σ polarization [5], and (iv) the in-plane transverse and longitudinal correlation lengths are identical [11,18]. Unless otherwise indicated, we therefore use σ polarization and focus on in-plane longitudinal $(h, 0)$ scans.

Temperature dependence of the charge scattering is shown in Figs. 2(a)–2(d), by plotting RIXS intensity distribution maps (IDMs)—intensity versus h and energy loss. The main experimental observation reported here is that the charge-stripe correlations in LESCO persist beyond the temperature onset reported by REXS [10,15,16] and even beyond the onset temperature of the LTT phase [Fig. 1(d)]. This is directly demonstrated by the raw RIXS IDMs as a function of temperature. Representative RIXS spectra measured with both the π and σ polarizations are shown in Figs. 2(e) and 2(f), respectively. The elastic charge scattering is drastically enhanced when cooling to base temperature [Fig. 2(e)] and by approaching $\mathbf{Q}_{\mathrm{CO}}$ [Fig. 2(f)].

To quantify the charge order intensity, these RIXS IDMs are analyzed as follows. Elastic scattering is inferred from each RIXS spectrum by integrating the intensity $\pm 2\sqrt{2 \ln 2}\sigma_G$ around the elastic line [see Fig. 2(e)]. To account for the variation of detection efficiency, the RIXS intensities are normalized to the weight of the *dd* excitations. In this fashion, after subtracting a linear background [17], longitudinal scans through $\mathbf{Q}_{\mathrm{CO}}$ [see Figs. 1(f), 2(g),

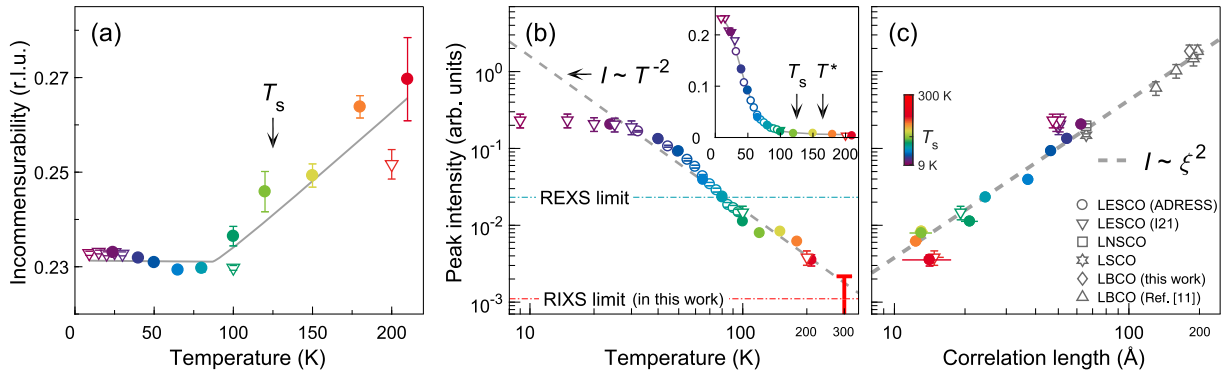

FIG. 3. Incommensurability, intensity, and correlation length of the charge-stripe order. (a), (b) Temperature dependence of the CO incommensurability (a) and peak intensity (b) in LESCO. The filled circles and open triangles in (b) denote the fitted amplitude of h scans obtained at ADRESS and I21, respectively. The open circles represent the background-subtracted elastic scattering intensity measured at $\mathbf{Q} = (0.235, 0)$. Backgrounds are measured at $\mathbf{Q} = (0.129, 0)$ and (0.346,0). The red vertical bar at 300 K illustrates the upper limit of the charge order peak height estimated from the h scan. The inset shows the same data on a linear scale. The REXS [10,15,16] and RIXS detection limits are indicated by horizontal dash-dotted lines. (c) CO peak intensity as a function of correlation length for LESCO, LNSCO, LBCO, and LSCO. Since the CO reflection in LSCO splits transversely into two peaks at low temperature (see Fig. S2(d) [17] and Ref. [12]), twice of the amplitude of a single peak is used for LSCO. The color code indicates the temperature for the LESCO data. Solid lines are guides to the eye.

and 2(h)] are generated. Gaussian fits of these scans allow us to extract (i) the scattering amplitude I, (ii) the incommensurability δ, and (iii) the in-plane correlation length ξ defined by the inverse half width at half maximum (HWHM). The temperature evolution of these parameters are summarized in Fig. 3.

The incommensurability is locked to $\delta \approx 0.23$ below 80 K. By contrast for $T > 80$ K, it increases upon warming and reaches $\delta \approx 0.27$ at $T = 210$ K [Fig. 3(a)]. The diffraction amplitude I decreases initially ($T < 30$ K) slowly before an approximately power-law T^{-2} decay [Fig. 3(b)]. As ξ decays in a similar fashion with temperature, plotting I versus ξ reveals a simple power-law relation between the two, i.e., $I \sim \xi^{\alpha}$ with $\alpha \approx 2.0$ [Fig. 3(c)]. The similar crystal field environment across La-based single-layer cuprates justifies comparison of CO diffraction intensities normalized to their respective dd excitations. Doing so, the $I \sim \xi^2$ scaling applies also to LNSCO, LBCO, and LSCO with doping $x = 1/8$ [see Fig. 3(c)].

We start by discussing how our RIXS experiments on LESCO compare to previous REXS reports [10,15,16]. The difference in charge ordering "onset" temperature found by, respectively, REXS and RIXS is a matter of probing sensitivity. With the energy resolving power of RIXS, it is possible to disentangle elastic from inelastic scattering processes [19]. As the diffraction amplitude from charge order is weakened upon increasing temperature, it eventually becomes negligible in comparison to, for example, dd excitations [Fig. 2(e)] [24]. In LESCO, this happens around $T \approx 80$ K, and hence this temperature scale marks the charge correlation detection limit for REXS experiments rather than a fundamental onset temperature. With differentiation of elastic and inelastic scattering processes, it is possible to probe the charge ordering response in LESCO in the regime beyond the REXS detection limit. The CO diffraction amplitude decays roughly as T^{-2} until the RIXS detection limit is reached between 200 and 300 K. Even more intriguingly, the in-plane integrated diffraction intensity remains essentially independent of temperature, i.e., $I \propto \xi^2$. Cooling into the pseudogap and LTT phases thus has no significant impact on the stripe order intensity. It is thus clear that the first order onset of LTT structure is neither triggering nor enhancing the stripe order in LESCO-1/8.

The scaling behavior of charge scattering ($I \propto \xi^2$) is reminiscent of the dynamic magnetic critical scattering in La_2CuO_4 and another $S = 1/2$ two-dimensional square-lattice quantum Heisenberg antiferromagnet (2DSLQHA) $Sr_2CuO_2Cl_2$ observed by neutron scattering experiments [31,32]. The amplitude of instantaneous spin correlations $S(\mathbf{q}) = S(0)/[1 + (\mathbf{q}/\xi)^2]$ is also found to scale with the spin correlation length as $S(0) \propto \xi^2$. Here, $\mathbf{q}$ is the two-dimensional deviation from the antiferromagnetic ordering wave vector. Notably, such scaling behavior observed on La_2CuO_4 is associated with two-dimensionality and local spin nature. However, it seems to be specific to the cuprates, as in copper formate tetradeuterate, another $S = 1/2$ 2DSLQHA, the ratio of $S(0)/\xi^2$ shows a clear temperature dependence [33]. As the response function for charge correlations is represented in the low-energy RIXS cross section [19,34], our experiments on stripe-ordered cuprates are analogous to the neutron scattering studies of La_2CuO_4. Drawing on this analog may suggest that critical charge correlations are probed.

The incommensurability δ in LESCO-1/8 is displaying, as in LBCO-1/8 [11,35], a strong temperature dependence. Below 80 K, a low-temperature lock-in of the incommensurability occurs. This lock-in temperature scale seems unrelated to the LTT structural transition. The fact that the incommensurability δ moves—with increasing temperature ($T > 80$ K)—from $\approx 1/4$ toward the $\approx 1/3$ found in $YBa_2Cu_3O_{7-y}$ (YBCO) [3–5,36,37], led to the suggestion that there exists a universal susceptibility for charge order correlations with $\delta \sim 0.3$ in hole-doped cuprates [11]. However, in LESCO the charge order incommensurability is not reaching $\delta = 0.3$ and hence the link to charge ordering in YBCO remains speculative. Future ultrahigh-resolution RIXS experiments should address whether the apparent shift in incommensurability is influenced by soft phonons or Kohn anomalies near $\mathbf{Q}_{CO}$ [38–40]. If such phonon excitations become relevant at high temperature, one would expect a broadening of the elastic CO peak. This is indeed observed, but there seems to be no obvious correlation between the broadening and incommensurability.

In both YBCO [41] and LBCO [35], the temperature dependence of the charge ordering has been analyzed using two components: a static long-range low-temperature and a fluctuating short-range high-temperature constituent. Our data on LESCO are analyzed with a single component that has a constant in-plane integrated intensity. Despite different analysis approaches, the low-temperature long-range correlations and integrated diffraction intensity can certainly be compared across 1/8-doped stripe-ordered compounds. The longest in-plane correlation lengths are found in LBCO [11,18], whereas more modest length scales are reported in LNSCO [1,18,20,21], LSCO [12], and LESCO (this work). Normalizing the best possible intensities across all these four compounds suggests a roughly constant in-plane integrated intensity (see Fig. S3 in Supplemental Material [17]) [42]. The fact that the LTT onset temperature and order parameter vary across these compounds [10,16,18] again suggests no link between the diffracted stripe order and the structural phase transition. It is also interesting to discuss correlation length and integrated diffracted intensity in the context of the Fermi surface reconstruction (FSR). In LBCO, LNSCO, and LESCO, the large low-temperature negative thermopower has been interpreted as evidence of a charge-stripe-order induced FSR [43,44]. This is supported by the fact that the negative thermopower is found in a dome around 1/8 doping [44]. Typically, the onset temperature T_{FSR} of the FSR is quantified by the zero crossing ($S = 0$) of the thermopower [44]. Both T_{FSR} and the zero-temperature thermopower values are essentially identical across these stripe-ordered compounds. The identical FSR onset temperature suggests that the in-plane correlation length is not the defining parameter for the FSR. Empirically, the in-plane integrated scattering intensity seems to be a more important parameter.

In summary, we have carried out resonant inelastic x-ray scattering experiments on stripe-ordered La-based cuprates. Focusing on LESCO-1/8, it is demonstrated—in contrast to previous elastic (resonant and nonresonant) reports—that stripe correlations precede the low-temperature tetragonal crystal structure. This permits us to conclude that stripe order generally emerges spontaneously without LTT structural deformations. While charge correlations in LESCO have been traced to the highest temperature among the stripe-ordered cuprates, the integrated scattering intensities are found to be compound independent. This, together with the temperature dependence of the diffraction amplitude, strongly suggests that stripe ordering in the cuprates goes beyond weak-coupling mean-field physics.

We thank T. M. Rice, L. Taillefer, M.-H. Julien, and M. Hücker for insightful discussion and Z. He and Y. Hao for assistance with XRD measurements. Q. W., M. H., K. v. A., C. E. M., Y. T., W. Z., T. S., and J. C. acknowledge support by the Swiss National Science Foundation through the SINERGIA network Mott Physics Beyond the Heisenberg Model and Grants No. BSSGI0-155873, No. P400P2_183890, and No. 200021-178867. Y. Sassa is funded by the Swedish Research Council (VR) with a Starting Grant (No. 2017-05078). Y. Shen and J. Z. were supported by the Innovation Program of Shanghai Municipal Education Commission (Grant No. 2017-01-07-00-07-E00018) and the National Key R&D Program of the MOST of China (Grant No. 2016YFA0300203). T. A. was supported by JSPS KAKENHI through Grant No. JP19H01841. N. B. C. thanks the Danish Agency for Science, Technology, and Innovation for funding the instrument center DanScatt. We acknowledge Swiss Light Source at the Paul Scherrer Institut, Diamond Light Source, and European Synchrotron Radiation Facility for approval of RIXS proposals at the ADRESS (No. 20182238), I21 (No. SP20828, MM24481), and ID32 (No. HC3888) beam lines, respectively.

*qisiwang@physik.uzh.ch
†johan.chang@physik.uzh.ch

[1] J. M. Tranquada, B. J. Sternlieb, J. D. Axe, Y. Nakamura, and S. Uchida, Nature (London) **375**, 561 (1995).
[2] Z. Zhang, R. Sutarto, F. He, F. C. Chou, L. Udby, S. L. Holm, Z. H. Zhu, W. A. Hines, J. I. Budnick, and B. O. Wells, Phys. Rev. Lett. **121**, 067602 (2018).
[3] J. Chang, E. Blackburn, A. T. Holmes, N. B. Christensen, J. Larsen, J. Mesot, R. Liang, D. A. Bonn, W. N. Hardy, A. Watenphul, M. v. Zimmermann, E. M. Forgan, and S. M. Hayden, Nat. Phys. **8**, 871 (2012).
[4] T. Wu, H. Mayaffre, S. Krämer, M. Horvatic, C. Berthier, W. N. Hardy, R. Liang, D. A. Bonn, and M.-H. Julien, Nature (London) **477**, 191 (2011).
[5] G. Ghiringhelli, M. L. Tacon, M. Minola, S. Blanco-Canosa, C. Mazzoli, N. B. Brookes, G. M. D. Luca, A. Frano,

D. G. Hawthorn, F. He, T. Loew, M. M. Sala, D. C. Peets, M. Salluzzo, E. Schierle, R. Sutarto, G. A. Sawatzky, E. Weschke, B. Keimer, and L. Braicovich, Science **337**, 821 (2012).
[6] M. Fujita, H. Goka, K. Yamada, J. M. Tranquada, and L. P. Regnault, Phys. Rev. B **70**, 104517 (2004).
[7] M. Hücker, M. v. Zimmermann, Z. J. Xu, J. S. Wen, G. D. Gu, and J. M. Tranquada, Phys. Rev. B **87**, 014501 (2013).
[8] M. Hücker, M. v. Zimmermann, G. D. Gu, Z. J. Xu, J. S. Wen, G. Xu, H. J. Kang, A. Zheludev, and J. M. Tranquada, Phys. Rev. B **83**, 104506 (2011).
[9] M. Hücker, M. v. Zimmermann, M. Debessai, J. S. Schilling, J. M. Tranquada, and G. D. Gu, Phys. Rev. Lett. **104**, 057004 (2010).
[10] A. J. Achkar, M. Zwiebler, C. McMahon, F. He, R. Sutarto, I. Djianto, Z. Hao, M. J. P. Gingras, M. Hücker, G. D. Gu, A. Revcolevschi, H. Zhang, Y.-J. Kim, J. Geck, and D. G. Hawthorn, Science **351**, 576 (2016).
[11] H. Miao, J. Lorenzana, G. Seibold, Y. Y. Peng, A. Amorese, F. Yakhou-Harris, K. Kummer, N. B. Brookes, R. M. Konik, V. Thampy, G. D. Gu, G. Ghiringhelli, L. Braicovich, and M. P. M. Dean, Proc. Natl. Acad. Sci. U.S.A. **114**, 12430 (2017).
[12] V. Thampy, M. P. M. Dean, N. B. Christensen, L. Steinke, Z. Islam, M. Oda, M. Ido, N. Momono, S. B. Wilkins, and J. P. Hill, Phys. Rev. B **90**, 100510(R) (2014).
[13] T. P. Croft, C. Lester, M. S. Senn, A. Bombardi, and S. M. Hayden, Phys. Rev. B **89**, 224513 (2014).
[14] N. B. Christensen, J. Chang, J. Larsen, M. Fujita, M. Oda, M. Ido, N. Momono, E. M. Forgan, A. T. Holmes, J. Mesot, M. Huecker, and M. v. Zimmermann, arXiv:1404.3192.
[15] J. Fink, E. Schierle, E. Weschke, J. Geck, D. Hawthorn, V. Soltwisch, H. Wadati, H.-H. Wu, H. A. Dürr, N. Wizent, B. Büchner, and G. A. Sawatzky, Phys. Rev. B **79**, 100502(R) (2009).
[16] J. Fink, V. Soltwisch, J. Geck, E. Schierle, E. Weschke, and B. Büchner, Phys. Rev. B **83**, 092503 (2011).
[17] See Supplemental Material at http://link.aps.org/supplemental/10.1103/PhysRevLett.124.187002 for details on experimental configurations, fitting of RIXS spectra, data normalization, background subtraction, temperature dependence of the inelastic spectral weight, and characterization of the LTT structural transition, which includes Refs. [8,11,12,18–26].
[18] S. B. Wilkins, M. P. M. Dean, J. Fink, M. Hücker, J. Geck, V. Soltwisch, E. Schierle, E. Weschke, G. Gu, S. Uchida, N. Ichikawa, J. M. Tranquada, and J. P. Hill, Phys. Rev. B **84**, 195101 (2011).
[19] L. J. P. Ament, M. van Veenendaal, T. P. Devereaux, J. P. Hill, and J. van den Brink, Rev. Mod. Phys. **83**, 705 (2011).
[20] M. v. Zimmermann, A. Vigliante, T. Niemöller, N. Ichikawa, T. Frello, J. Madsen, P. Wochner, S. Uchida, N. H. Andersen, J. M. Tranquada, D. Gibbs, and J. R. Schneider, Europhys. Lett. **41**, 629 (1998).
[21] J. Kim, H. Zhang, G. D. Gu, and Y.-J. Kim, J. Supercond. Novel Magn. **22**, 251 (2009).
[22] L. J. P. Ament, G. Ghiringhelli, M. M. Sala, L. Braicovich, and J. van den Brink, Phys. Rev. Lett. **103**, 117003 (2009).
[23] M. W. Haverkort, Phys. Rev. Lett. **105**, 167404 (2010).
[24] M. M. Sala, V. Bisogni, C. Aruta, G. Balestrino, H. Berger, N. B. Brookes, G. M. de Luca, D. D. Castro, M. Grioni, M. Guarise, P. G. Medaglia, F. M. Granozio, M. Minola, P. Perna, M. Radovic, M. Salluzzo, T. Schmitt, K. J. Zhou, L. Braicovich, and G. Ghiringhelli, New J. Phys. **13**, 043026 (2011).
[25] H. Kimura, H. Goka, M. Fujita, Y. Noda, K. Yamada, and N. Ikeda, Phys. Rev. B **67**, 140503(R) (2003).
[26] B. Simovič, M. Hücker, P. C. Hammel, B. Büchner, U. Ammerahl, and A. Revcolevschi, Phys. Rev. B **67**, 224508 (2003).
[27] O. Cyr-Choinière, R. Daou, F. Laliberté, C. Collignon, S. Badoux, D. LeBoeuf, J. Chang, B. J. Ramshaw, D. A. Bonn, W. N. Hardy, R. Liang, J.-Q. Yan, J.-G. Cheng, J.-S. Zhou, J. B. Goodenough, S. Pyon, T. Takayama, H. Takagi, N. Doiron-Leyraud, and L. Taillefer, Phys. Rev. B **97**, 064502 (2018).
[28] G. Ghiringhelli, A. Piazzalunga, C. Dallera, G. Trezzi, L. Braicovich, T. Schmitt, V. N. Strocov, R. Betemps, L. Patthey, X. Wang, and M. Grioni, Rev. Sci. Instrum. **77**, 113108 (2006).
[29] V. N. Strocov, T. Schmitt, U. Flechsig, T. Schmidt, A. Imhof, Q. Chen, J. Raabe, R. Betemps, D. Zimoch, J. Krempasky, X. Wang, M. P. A. Grioni, and L. Patthey, J. Synchrotron Radiat. **17**, 631 (2010).
[30] Y. Y. Peng, A. A. Husain, M. Mitrano, S. Sun, T. A. Johnson, A. V. Zakrzewski, G. J. MacDougall, A. Barbour, I. Jarrige, V. Bisogni, and P. Abbamonte, arXiv:1910.05526.
[31] R. J. Birgeneau, M. Greven, M. A. Kastner, Y. S. Lee, B. O. Wells, Y. Endoh, K. Yamada, and G. Shirane, Phys. Rev. B **59**, 13788 (1999).
[32] M. Greven, R. J. Birgeneau, Y. Endoh, M. A. Kastner, M. Matsuda, and G. Shirane, Z. Phys. B **96**, 465 (1995).
[33] H. M. Rønnow, D. F. McMorrow, and A. Harrison, Phys. Rev. Lett. **82**, 3152 (1999).
[34] C. Jia, K. Wohlfeld, Y. Wang, B. Moritz, and T. P. Devereaux, Phys. Rev. X **6**, 021020 (2016).
[35] H. Miao, R. Fumagalli, M. Rossi, J. Lorenzana, G. Seibold, F. Yakhou-Harris, K. Kummer, N. B. Brookes, G. D. Gu, L. Braicovich, G. Ghiringhelli, and M. P. M. Dean, Phys. Rev. X **9**, 031042 (2019).
[36] A. J. Achkar, R. Sutarto, X. Mao, F. He, A. Frano, S. Blanco-Canosa, M. Le Tacon, G. Ghiringhelli, L. Braicovich, M. Minola, M. Moretti Sala, C. Mazzoli, R. Liang, D. A. Bonn, W. N. Hardy, B. Keimer, G. A. Sawatzky, and D. G. Hawthorn, Phys. Rev. Lett. **109**, 167001 (2012).
[37] M. Hücker, N. B. Christensen, A. T. Holmes, E. Blackburn, E. M. Forgan, R. Liang, D. A. Bonn, W. N. Hardy, O. Gutowski, M. v. Zimmermann, S. M. Hayden, and J. Chang, Phys. Rev. B **90**, 054514 (2014).
[38] E. Blackburn, J. Chang, A. H. Said, B. M. Leu, R. Liang, D. A. Bonn, W. N. Hardy, E. M. Forgan, and S. M. Hayden, Phys. Rev. B **88**, 054506 (2013).
[39] M. Le Tacon, A. Bosak, S. M. Souliou, G. Dellea, T. Loew, R. Heid, K.-P. Bohnen, G. Ghiringhelli, M. Krisch, and B. Keimer, Nat. Phys. **10**, 52 (2014).
[40] D. Reznik, L. Pintschovius, M. Ito, S. Iikubo, M. Sato, H. Goka, M. Fujita, K. Yamada, G. D. Gu, and J. M. Tranquada, Nature (London) **440**, 1170 (2006).

[41] R. Arpaia, S. Caprara, R. Fumagalli, G. De Vecchi, Y. Y. Peng, E. Andersson, D. Betto, G. M. De Luca, N. B. Brookes, F. Lombardi, M. Salluzzo, L. Braicovich, C. Di Castro, M. Grilli, and G. Ghiringhelli, Science **365**, 906 (2019).

[42] The previous REXS work in Ref. [18] suggests that the in-plane integrated charge ordering intensity in LBCO is ∼10 times larger than that in LNSCO. However, we note that compared to the current work and other studies [20,21], a much larger in-plane correlation length ($\xi = 111 \pm 7$ Å) of charge order in LNSCO is reported in Ref. [18].

[43] J. Chang, R. Daou, C. Proust, D. LeBoeuf, N. Doiron-Leyraud, F. Laliberté, B. Pingault, B. J. Ramshaw, R. Liang, D. A. Bonn, W. N. Hardy, H. Takagi, A. B. Antunes, I. Sheikin, K. Behnia, and L. Taillefer, Phys. Rev. Lett. **104**, 057005 (2010).

[44] F. Laliberté, J. Chang, N. Doiron-Leyraud, E. Hassinger, R. Daou, M. Rondeau, B. J. Ramshaw, R. Liang, D. A. Bonn, W. N. Hardy, S. Pyon, T. Takayama, H. Takagi, I. Sheikin, L. Malone, C. Proust, K. Behnia, and L. Taillefer, Nat. Commun. **2**, 432 (2011).

Supplemental Material for
High-Temperature Charge-Stripe Correlations in $La_{1.675}Eu_{0.2}Sr_{0.125}CuO_4$

Q. Wang *et al.*

I. SCATTERING GEOMETRY AND RIXS CROSS-SECTION

The scattering geometry of the RIXS experiments are given in Fig. 1(c) and Table S1. At certain photon energy, the magnitude of total momentum transfer $|\mathbf{Q}|$ is determined by the scattering angle γ. By changing the incident angle θ and sample azimuthal angle ϕ, the in-plane component $\mathbf{Q}_{\parallel}$ can be varied. The range of ℓ covered in each measurement and the value (ℓ_0) at the in-plane charge ordering wavevector at base temperature are shown in Table S1.

The RIXS intensity (proportional to cross-section) from initial state $|i\rangle$ to final state $|f\rangle$ can be expressed by the Kramers-Heisenberg equation [1]:

$$I_{fi}(\epsilon,\epsilon') \propto \left| \sum_n \frac{\left\langle f \left| D^{\dagger}_{\epsilon'} \right| n \right\rangle \langle n | D_{\epsilon} | i \rangle}{E_i - E_n + \hbar\omega_k + i\Gamma_n/2} \right|^2 \delta\left(E_i - E_f + \hbar\omega_k - \hbar\omega'_k\right) \tag{1}$$

where ω_k, ϵ (ω'_k, ϵ') are the energy and momentum of the incident (scattered) photon. D_ϵ ($D_{\epsilon'}$) is the polarization dependent dipole operator. E_i, E_f and E_n are the energy of initial, final and intermediate state $|n\rangle$. Γ_n is the inverse core-hole lifetime. The resonant scattering is enhanced when the incident photon is in resonance with a specific transition in the sample *i.e.* $\hbar\omega_k \approx E_n - E_i$.

In the case of scattering from charge order, the RIXS intensity is dominated by the polarization preserving elastic scattering processes ($\sigma \to \sigma$, $\pi \to \pi$). Under the single ion approximation, we obtain the amplitude for such scattering with σ and π polarized incident x-ray [2, 3]:

$$I(\sigma,\sigma) = I_0[1 + \frac{1}{4}\sin^2(\alpha - \frac{\gamma}{2})\cos^2\theta_{\text{spin}}] \tag{2}$$

$$I(\pi,\pi) = I_0 \sin^2(\alpha + \frac{\gamma}{2})[\sin^2(\alpha - \frac{\gamma}{2}) + \frac{1}{4}\cos^2\theta_{\text{spin}}] \tag{3}$$

where α is the angle between total momentum transfer $\mathbf{Q}$ and its out-of-plane component $\mathbf{Q}_{\perp}$. θ_{spin} is the angle between the spin and sample c-axis direction. In underdoped cuprates, it is assumed that $\theta_{\text{spin}} \approx 90°$. Then the polarization preserving elastic scattering amplitude becomes identical for the grazing-incidence ($\alpha < 0$) and grazing-exit ($\alpha > 0$) geometry with fixed $|\mathbf{Q}_{\parallel}|$.

From our RIXS data on LESCO and LSCO, we determine the ratio between charge order diffraction amplitude with σ and π polarized incident x-ray to be $I(\sigma,\sigma)/I(\pi,\pi) \approx 2.7$ [see Fig. 1(f)] and ≈ 2.8 [see Fig. S2(d)], respectively. These results are in good agreement with the theoretical value $I(\sigma,\sigma)/I(\pi,\pi) \approx 2.6$ calculated using Eq. (2) and (3). The scattering geometry dependence of the *dd*-excitation intensity is more complicated [4]. However, with all our experimental configurations, we estimate the variation of the integrated intensity of *dd* excitations to be within $\sim 20\%$. To account for this, an error of 20% is added when data are normalized across different instruments/polarizations.

Table S 1. Summary of RIXS experimental configurations.

Sample	$a \approx b$ (Å)	c (Å)	Beamline	$\sigma_{\rm G}$ (meV)	γ (°)	ℓ (r.l.u.)	ℓ_0 (r.l.u.)	Pol. (in)	Grazing in/exit	T (K)
LESCO	3.79	13.1	ADRESS	48	130	1.33–1.73	1.59	σ, π	exit	24–210
			I21	19	154	1.47–1.86	1.74	σ, π	exit	9–300
LNSCO	3.78	13.1	ADRESS	54	130	1.26–1.68	1.55	σ	in	16
LBCO	3.78	13.2	ID32	48	114–125	1.50	1.50	π	exit	20
LSCO	3.78	13.2	ADRESS	56	130	1.59	1.59	σ, π	exit	20

II. FITTING OF RIXS SPECTRA

The zero energy loss is determined by fitting the low-energy part of each RIXS spectrum. We describe the elastic scattering by a Gaussian profile where the width is set by the instrumental energy resolution (orange lines in Fig. S1). This energy resolution thus represents a technique-specific upper bound of the time scale below which fluctuations are considered as "static". The low-energy inelastic scattering is dominated by magnetic excitations. A damped harmonic oscillator is adopted to model the imaginary part of the spin dynamic susceptibility:

$$\chi''(\mathbf{Q},\omega) = \frac{\chi_0''}{2\omega_0}\left[\frac{\Gamma/2}{(\omega-\omega_0)^2+(\Gamma/2)^2} - \frac{\Gamma/2}{(\omega+\omega_0)^2+(\Gamma/2)^2}\right] \tag{4}$$

The corresponding RIXS intensity from magnetic scattering $S(\mathbf{Q},\omega)$ is given by:

$$S(\mathbf{Q},\omega) = \frac{\chi''(\mathbf{Q},\omega)}{1-e^{-\hbar\omega/k_{\rm B}T}} \tag{5}$$

where $\hbar$ is the reduced Planck constant and $k_{\rm B}$ is the Boltzmann constant. We have convoluted $S(\mathbf{Q},\omega)$ with the energy resolution function. The resulting profile is depicted by the green lines in Fig. S1. A quadratic function is added to mimic the background (BG). The quality of fitting can be appreciated in Fig. S1 and Fig. 2(f). The same analysis protocol was used in Ref. [5].

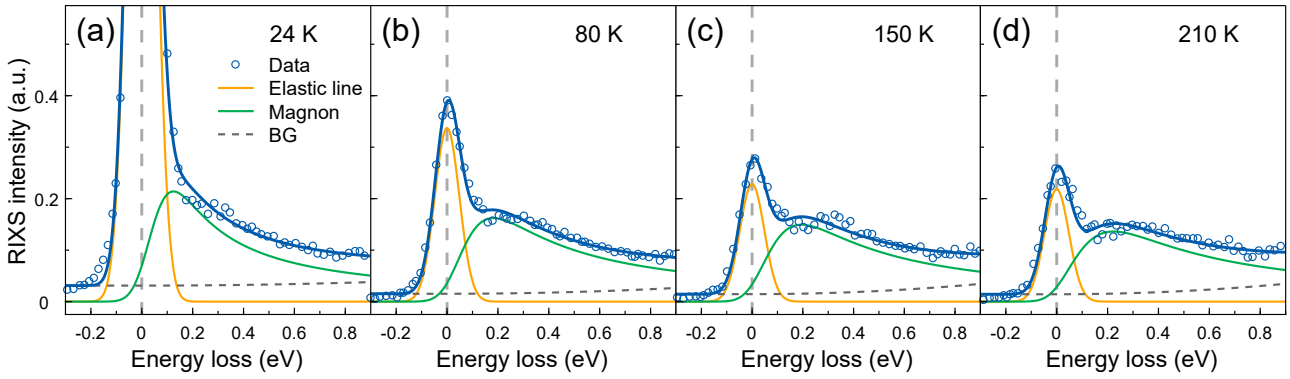

Figure S 1. **Raw RIXS spectra in LESCO.** Representative raw RIXS spectra at $\mathbf{Q}_{\rm CO}$ at (a) 24 K, (b) 80 K, (c) 150 K and (d) 210 K with fits and each fitted component.

III. RAW DATA, NORMALIZATION AND INTEGRATION OF DIFFRACTION INTENSITIES

Figs. S2(a)–S2(d) show representative raw data of the elastic **Q**-scans measured on LESCO, LNSCO, LBCO and LSCO, respectively. The **Q**-scans presented in the manuscript are obtained by subtracting linear backgrounds.

For a direct comparison between different samples, the charge order scattering intensities are normalized to the area of *dd* excitations. Data obtained with π polarization are given a geometric scaling factor according to the discussion in the previous section. The modulation of the charge order intensity $I(\ell)$ along ℓ, weak though, is also considered in the normalization using the relation $I(\ell) \propto \sin^2(\pi\ell)$ [6, 7]. The difference between the self-absorption coefficients for each experimental setup has been corrected following the procedure discussed in detail in the Supporting Information of Ref. [5]. In general, the self-absorption effect is minimized with grazing incidence geometry. This leads to an enhancement of raw elastic intensity in LNSCO where grazing incidence geometry was adopted [Fig. S2(b)]. The normalization processes are justified by the following facts. *(i)* The crystal field environments are similar across La-based single-layer cuprates. *(ii)* The energy window of elastic intensity integration is always set by the experimental energy resolution. Results on the same LESCO sample obtained at two instruments show good consistency [see Figs. 2(g), 2(h) and 3]. We have therefore normalized the I21 data to the ADRESS data by the peak amplitudes at the overlapping temperature (24–25 K). Charge order intensities in LBCO from Ref. [5] are normalized to the amplitude of *h*-scan at base temperature of this work. We note that in Ref. [5], two components are used to analyze the charge order peak in LBCO. To avoid complexity, in our analysis we have only included data from Ref. [5] measured below 40 K where the low-temperature component dominates charge order scattering intensity.

While charge orders in all La-1/8 compounds share roughly a constant in-plane integrated intensity (Fig. S3), their low-temperature diffraction peaks are found to be best described by different profiles: A Gaussian function is used to fit the longitudinal scans in LESCO and LNSCO [Figs. S2(a) and S2(b)]; a Lorentzian-squared function for the longitudinal scans in LBCO [Fig. S2(c) and Ref. [5]]; and a function comprising two Gaussians of equal width and height for the azimuthal scan (approximately along the transverse direction) in LSCO [Fig. S2(d)]. The correlation lengths extracted from these fittings are consistent with previous reports [5, 8, 9]. In LESCO, LNSCO and LBCO, the charge order peak is isotropic in the *hk*-plane [5, 10], while in LSCO it can be viewed as two split isotropic peaks [9].

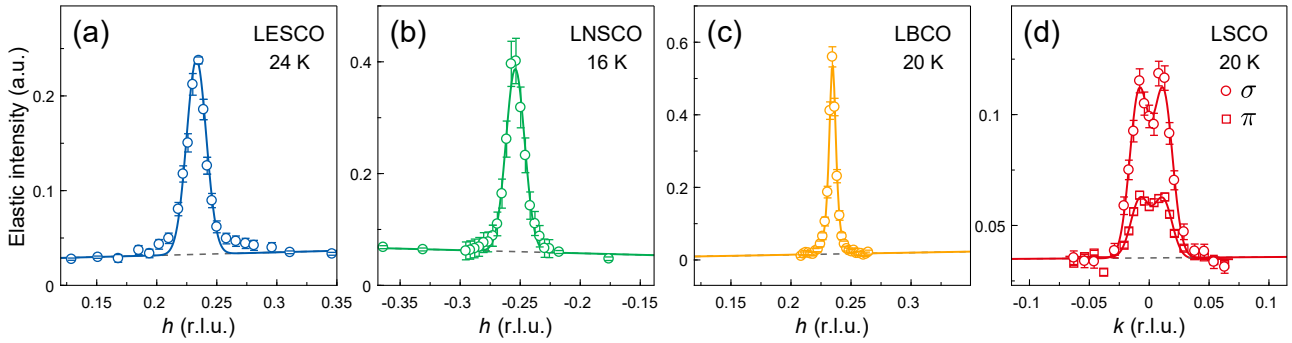

Figure S 2. Raw data of the elastic Q-scans through the charge order peak. (a), (b) Raw *h*-scans measured on (a) LESCO and (b) LNSCO with σ polarization. (c) Raw *h*-scan measured on LBCO with π polarization. (d) Raw azimuthal scans (ϕ-scans) measured on LSCO with both σ and π polarizations. The solid lines are fits to the raw data. The dashed lines indicate backgrounds. Error bars are three times the standard deviations. Data for LSCO with π polarization have been shifted vertically for clarity.

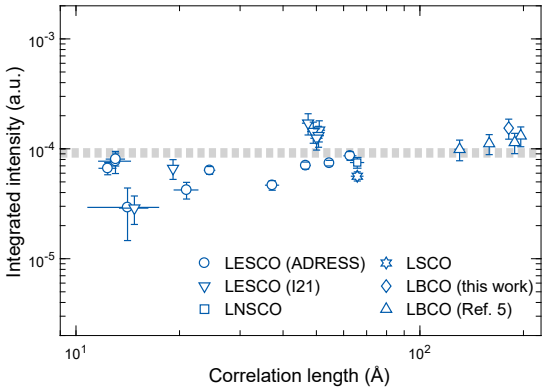

Figure S 3. In-plane integrated intensity of the charge order scattering versus correlation length for different La-1/8 compounds.

Based on these facts, we extend the peak profiles into their two-dimensional forms and calculate the peak volume as the in-plane integrated intensity of the charge order diffraction.

IV. ENERGY RESOLUTION OF THE RIXS SPECTROMETERS

We used spectra recorded on amorphous carbon tape to evaluate the energy resolution. Elastic scattering from the carbon tape overwhelms largely any inelastic component. It thus provides the most clear-cut extraction of the effective energy resolution. An example profile from the I21 instrument at the Diamond synchrotron is shown in Fig. S4. This profile is fitted to a Gaussian, Lorentzian and Voigt function, respectively. In this fashion, it is shown that the lineshape is predominately Gaussian. The additional fitting parameters included into the Voigt function, although improving the fitting of the low-intensity tail, do not lead to a significant correction to the evaluation of the energy resolution. In Table S1, we therefore parameterize the energy resolution by the Gaussian standard deviation. A Gaussian profile is also used for the fitting of elastic scattering in the spectra recorded on the stripe-ordered samples.

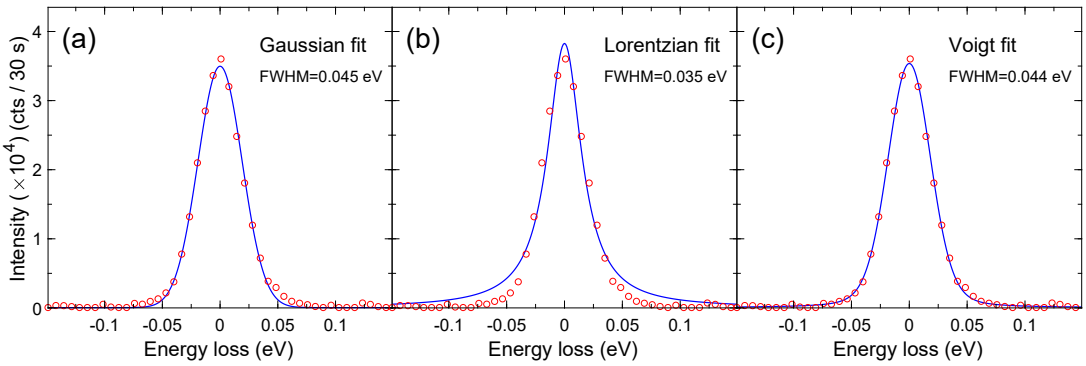

Figure S 4. RIXS spectrum recorded on amorphous carbon tape. (a)–(c) The same spectrum for which the elastic line is fitted to a Gaussian, Lorentzian and Voigt function, respectively. The profile is to a good approximation described by a Gaussian lineshape and naturally the additional fitting parameters included in the Voigt function lead to a further improvement.

V. TEMPERATURE DEPENDENCE OF INELASTIC SPECTRAL WEIGHT.

At base temperature, elastic scattering from the charge-stripe order largely dominates over the inelastic sector. With increasing temperature, this elastic signal weakens and eventually becomes comparable first to the *dd* excitations and ultimately to the response of spin excitations. It is therefore important to characterize the temperature dependence of the spin-excitation spectral weight. For illustration purpose, we are using data recorded at the ADRESS instrument with an energy resolution of $\sigma_{\mathrm{G}} \sim 48$ meV. In Fig. S5, we integrated the spin excitation spectral weight in the window of 200–500 meV. By being more than four Gaussian standard deviations away from the elastic line, the weight is surely dominated by inelastic processes. Notice that for $\mathbf{Q} = \mathbf{Q}_{\mathrm{CO}}$ this statement is only getting more accurate as temperature is increased. Whether being at $\mathbf{Q} = (0.235, 0)$ (near $\mathbf{Q}_{\mathrm{CO}}$) or at $\mathbf{Q} = (0.346, 0)$ (background), an approximate constant high-temperature tail is observed. Similar spectral weight conservation is expected from phonons. On this basis, we exclude that inelastic processes can be responsible for the decaying elastic intensity found at $\mathbf{Q}_{\mathrm{CO}}$.

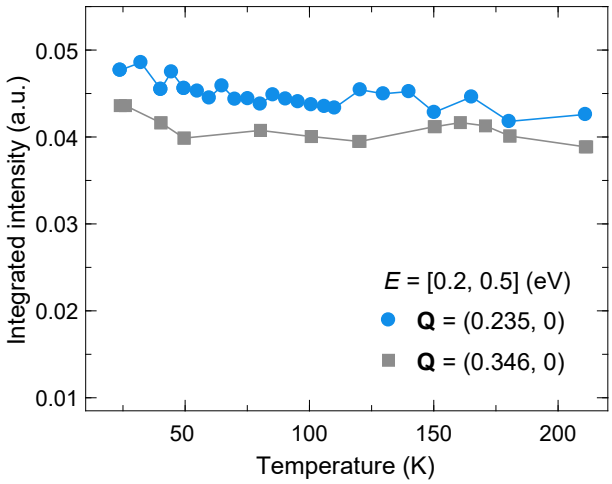

Figure S 5. Integrated inelastic spectral weight versus temperature. For $\mathbf{Q} = (0.235, 0)$ and $\mathbf{Q} = (0.346, 0)$, inelastic intensity is integrated in the window 200–500 meV. Overall only weak variations are found and in the temperature range 100–200 K, the intensity is approximately constant.

VI. TRANSITION FROM LTO TO LTT CRYSTAL STRUCTURE.

As in $La_{2-x}Ba_xCuO_4$ and $La_{1.6-x}Nd_{0.4}Sr_xCuO_4$, the $La_{1.8-x}Eu_{0.2}Sr_xCuO_4$ also undergoes a structural transition from low-temperature orthorhombic (LTO) to low-temperature tetragonal (LTT) structure. The highest transition temperature $\sim$ 125 K is found in the $La_{1.8-x}Eu_{0.2}Sr_xCuO_4$. Fig. 1(d) displays the $(3, 0, 0)$ Bragg peak – that is allowed in LTT phase but forbidden in the LTO structure – as a function of temperature. As expected, the amplitude of the $(3, 0, 0)$ Bragg peak drops to zero around the LTT to LTO transition. In Fig. S6, the $(2, 2, 0)$ Bragg peak is shown as a function of temperature. Above the structural transition, the $(2, 2, 0)$ Bragg peak is split due to the orthorhombicity. The orthorhombic splitting drops sharply to zero at the transition temperature. As there are no continuous connection between the lattice distortions in the LTO and LTT phase, the structural phase transition is

first order in agreement with our and published data [11, 12]. Since there is no evidence of a first order transition in the scattering amplitude from the charge order, there is no direct proportionality between the $(3, 0, 0)$ LTT Bragg peak and the stripe order in $La_{1.8-x}Eu_{0.2}Sr_xCuO_4$.

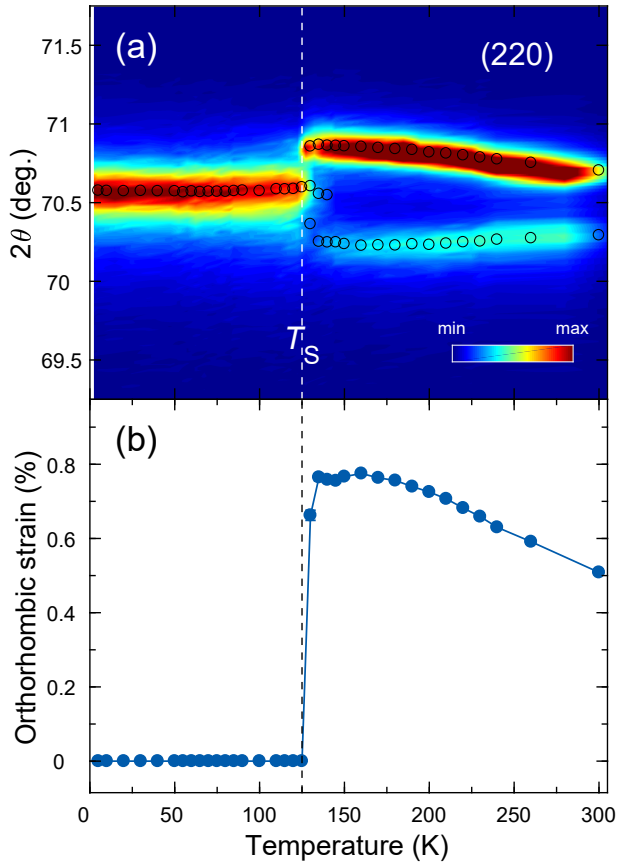

Figure S 6. LTO to LTT transition observed through the $(2, 2, 0)$ Bragg peak. (a) False color map of diffracted intensity versus temperature and scattering angle 2θ across the $(2, 2, 0)$ Bragg reflection. The open circles denote the peak positions fitted from the longitudinal scans. For consistency, notation in the HTT phase is used. (b) Orthorhombic order parameter – defined by $2(b_o - a_o)/(a_o + b_o)$ where a_o and b_o are the lattice constants in the orthorhombic phase – versus temperature.

[1] L. J. P. Ament, M. van Veenendaal, T. P. Devereaux, J. P. Hill, and J. van den Brink, Rev. Mod. Phys. **83**, 705 (2011).

[2] L. J. P. Ament, G. Ghiringhelli, M. M. Sala, L. Braicovich, and J. van den Brink, Phys. Rev. Lett. **103**, 117003 (2009).

[3] M. W. Haverkort, Phys. Rev. Lett. **105**, 167404 (2010).

[4] M. M. Sala, V. Bisogni, C. Aruta, G. Balestrino, H. Berger, N. B. Brookes, G. M. de Luca, D. D. Castro, M. Grioni, M. Guarise, P. G. Medaglia, F. M. Granozio, M. Minola, P. Perna, M. Radovic, M. Salluzzo, T. Schmitt, K. J. Zhou, L. Braicovich, and G. Ghiringhelli, New J. Phys. **13**, 043026 (2011).

[5] H. Miao, J. Lorenzana, G. Seibold, Y. Y. Peng, A. Amorese, F. Yakhou-Harris, K. Kummer, N. B. Brookes, R. M. Konik, V. Thampy, G. D. Gu, G. Ghiringhelli, L. Braicovich, and M. P. M. Dean, Proc. Natl. Acad. Sci. **114**, 12430 (2017).

[6] M. v. Zimmermann, A. Vigliante, T. Niemöller, N. Ichikawa, T. Frello, J. Madsen, P. Wochner, S. Uchida, N. H. Andersen, J. M. Tranquada, D. Gibbs, and J. R. Schneider, Europhys. Lett. **41**, 629 (1998).

[7] H. Kimura, H. Goka, M. Fujita, Y. Noda, K. Yamada, and N. Ikeda, Phys. Rev. B **67**, 140503(R) (2003).

[8] J. Kim, H. Zhang, G. D. Gu, and Y.-J. Kim, J. Supercond. Nov. Magn. **22**, 251 (2009).

[9] V. Thampy, M. P. M. Dean, N. B. Christensen, L. Steinke, Z. Islam, M. Oda, M. Ido, N. Momono, S. B. Wilkins, and J. P. Hill, Phys. Rev. B **90**, 100510(R) (2014).

[10] S. B. Wilkins, M. P. M. Dean, J. Fink, M. Hücker, J. Geck, V. Soltwisch, E. Schierle, E. Weschke, G. Gu, S. Uchida, N. Ichikawa, J. M. Tranquada, and J. P. Hill, Phys. Rev. B **84**, 195101 (2011).

[11] M. Hücker, M. v. Zimmermann, G. D. Gu, Z. J. Xu, J. S. Wen, G. Xu, H. J. Kang, A. Zheludev, and J. M. Tranquada, Phys. Rev. B **83**, 104506 (2011).

[12] B. Simovič, M. Hücker, P. C. Hammel, B. Büchner, U. Ammerahl, and A. Revcolevschi, Phys. Rev. B **67**, 224508 (2003).